

Computational materials chemistry at the nanoscale

Tahir Çağın*, Jianwei Che, Yue Qi, Yanhua Zhou, Ersan Demiralp, Guanghua Gao, and William A. Goddard III*
*Materials and Process Simulation Center, Beckman Institute (139-74), Division of Chemistry and Chemical Engineering, California Institute of Technology, Pasadena, CA 91125, USA; *Authors for correspondence*

Received 17 July 1998; accepted 9 November 1998

Key words: multiscale simulations, nanoscale applications, molecular dynamics, force fields, nanorheology, nanowires

Abstract

In order to illustrate how atomistic modeling is being used to determine the structure, physical, and chemical properties of materials at the nanoscale, we present here the results of molecular dynamics (MD) simulations on nanoscale assemblies of such materials as carbon nanotubes, diamond surfaces, metal alloy nanowires, and ceramics. We also include here the results of nonequilibrium MD simulations on the nanorheology of a monolayer of wear inhibitor self-assembled on two metal oxide surfaces, separated by hexadecane lubricant, and subjected to steady state shear.

We also present recent developments in force fields (FF) required to describe bond breaking and phase transformations in such systems. We apply these to study of plasticity in metal alloy nanowires where we find that depending on the strain rate, the wire may deform plastically (forming twins), neck and fracture, or transition to the amorphous phase.

1. Introduction

Nanotechnology, as defined in this paper, is concerned with the structures, properties, and processes involving materials having organizational features on the spatial scale of 1–300 nm. At this scale devices may lead to dramatically enhanced performance, sensitivity, and reliability with dramatically decreased size, weight, and cost. Indeed these scales can lead to new phenomena providing opportunities for new levels of sensing, manipulation, and control. However, being much smaller than the wavelength of visible light but much larger than simple molecules, it is difficult to characterize the structure and to control the processes involving nanomaterials. From the experimental point of view, the fundamental problem in the nanoscale region is that the *units are too small to see* and manipulate and too large for single pot synthesis from chemical precursors. Because it is difficult to *see* what we

are doing at the nanoscale, it is essential to develop theoretical and computational approaches sufficiently fast and accurate that the structure and properties of materials can be predicted for various conditions (temperature, pressure, concentrations) as a function of time.

1.1. *The multiscale computational hierarchical strategy for materials simulations*

A particular advantage of using theory is that the properties of new materials can be predicted in advance of experiments. This allows the system to be adjusted and refined (designed) so as to obtain the optimal properties before the arduous experimental task of synthesis and characterization. However, there are significant challenges in using theory to predict accurate properties for nanoscale materials. Thus, a cube of polyethylene (PE) 100 nm on side would have ~64 million atoms, much

too large for standard classical molecular dynamics (MD) and enormously too large for quantum mechanics (QM). Consequently, we use the *multiscale computational (MSC) hierarchical strategy* illustrated in Figure 1. The idea here is to start with accurate first principles QM on small system (10s or 100s of atoms) at a level sufficient to describe bond breaking and formation processes (reactions). Based on the QM results, we then find force fields (FF) to replace the electrons in terms of springs. As described below, it is now possible for FF to describe reaction processes accurately. Using the FF allows classical MD simulations with 1000s of atoms. With current methods and hardware, MD is practical up to ~ 1 million atoms, but a million atoms of PE is a cube of only ~ 25 nm on a side. To treat much larger systems, it is essential to average the atoms into collective units (segments, grains, pseudoatoms). This is the mesoscale region at the heart of nanoscale technology. Progress is being made in mesoscale simulations, but the demands of nanoscale technology require many additional advances. The simulations at the mesoscale can then be used to determine the parameters for finite element grids used in continuum calculations.

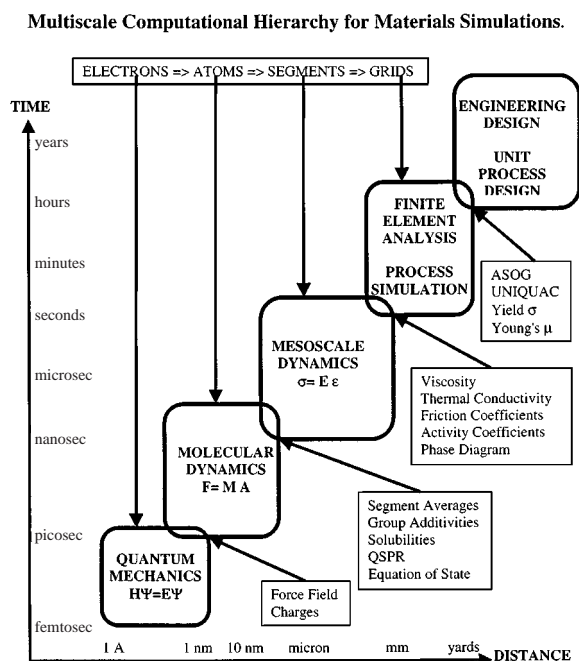


Figure 1. The multiscale computational hierarchy of materials simulators.

1.2. Nanoscale applications

Nanophase materials may include carbon nanotubes, fullerenes, dendrimers, ceramics, zeolites, semiconductors, metals, polymers, and liquid crystals. These might be in the vapor/gas, liquid or solid phase (or all three phases may be present and interacting through vapor–liquid, solid–liquid, vapor–solid interfaces). The properties one needs to predict include:

Structural properties: Internal structure (bond topology, distances and angles), morphology, microstructure
Mechanical properties: Vibrational modes, elastic moduli, yield limits, strength, toughness, temperature and pressure effects on mechanical properties (plasticity, yield, fracture, creep)

Surface properties: Reconstruction, oxidation, adhesion, friction, and wear

Transport properties: Diffusion and thermal conductivity

Rheological properties: Viscosity and flow of fluids in the nanoscale regime, non-Newtonian behavior, flow and transport properties of nanoparticles to make electro-rheological or magneto-rheological fluids, structure–fluid interactions and their effect on transport properties, time, and frequency dependence of the flow properties.

Section 4 presents example applications including nanotubes (Sections 4.1, 4.2, 4.3), predictions of friction (Sections 4.4, 4.5) and viscosity (Section 4.5), describing plastic flow in nanowires (Section 4.6), and phase transitions (Section 4.7).

Predicting the structure, dynamics, and properties at the nanoscale regimes requires substantial improvements in theory (FF and simulation methodologies) and the software (the algorithms implementation to do the calculations). Sections 2 and 3 describes some recent developments in theory, FF, and simulation approaches that underly the applications to nanoscale systems.

2. Methods for simulating nanoscale materials (electrons to atoms and beyond)

Modeling, simulation, and design of nanophase materials involves various levels of theory: QM, FF development, MD, and meso-scale methods.

2.1. Quantum mechanics

QM is the foundation for the theoretical description of materials. QM is particularly important for describing

processes in which bonds are broken and formed. Only with QM can one be sure to obtain accurate barrier heights and bond energies. Consequently our group first concentrated on developing quantum mechanical methods (GVB,¹ PS-GVB,² MR-CI,³ GDS-DFT⁴) capable of giving accurate barriers for the reactions of nanoscale materials. There has been tremendous progress in such first principles electronic structure methods; however, the calculations are often far too slow for studying the applications of interest to nanotechnology.

2.2. Force fields

In order to allow practical calculations on large systems, we want to average over electrons from QM to obtain a FF that can describe the energy and forces in terms of atomic positions. Using results from QM we can develop FF adequate for predicting the energetics needed to simulate the structure and properties of nanophase materials. The FF must even be accurate enough to obtain the correct energy differences for different phases of materials but must also describe the intermediate structures involved in phase transformations and interfacial phenomena. Standard FF generally use simple springs to represent bonds and angles in describing structures and vibrations of molecules. Such simple FF generally do not accurately describe the vibrational properties of molecules, which require cross terms and more complicated springs. The best FF are fit to the QM using the Hessian-Biased FF (HBFF)⁵ approach, which allows experimental information (about frequencies, polarizabilities, etc.) to be combined with normal mode information from QM. This HBFF approach has been used to develop accurate FF for polymers (e.g., PE, PVDF, nylon, POM, SiH),^{6–11} ceramics and semiconductors,^{12,13} and metals.^{14,15}

On the other hand, for fast qualitative considerations of new systems, we find generic FF suitable for general classes of systems to be quite useful. This includes the DREIDING FF¹⁶ (for the main group elements) and the Universal force field (UFF)¹⁷ (all elements: any inorganic, organo-metallic, or organic molecules).

In recent years, critical advances have been made in developing FF for describing:

- i. metals, where many body interactions play critical role on their physical properties;
- ii. oxides, ceramics, and zeolites, where competition between ionic and covalent bonding is very

important, especially in describing polymorphic phase transitions, reactions, defects, surface, and interface properties;

- iii. covalent bonded system such as carbon, hydrocarbons, silicon, germanium and their behavior far from equilibrium where the description of bond breaking and formation must be included to obtain an accurate description.

Section 3.0 will describe some new developments in classical FF to describe reactions (bond breaking and forming) and changes in ligancy and coordination for various types of systems.^{18–22}

2.3. Molecular dynamics

Given the FF to predict the forces, we can solve the coupled sets of Newton's equations to describe the motion of the N interacting atoms, this is referred to as MD. One can then connect the trajectories ($\mathbf{R}_i, \mathbf{V}_i; i = 1, N$) generated by the MD to obtain macroscopic properties through the use of statistical mechanics and thermodynamics.^{23–26} MD simulations of heterogeneous nanophase materials may require thousands to millions of atoms to be considered explicitly. Accurate evaluation of the long-range interactions (electrostatic and dispersion), which decrease slowly with distance, is the most time-consuming aspect for MD simulations of such large systems. This cost is order (N^2) for N particles. Thus, a system of 10 million atoms requires the evaluation of 10^{14} terms each time step. The standard approach to simplifying such calculations for finite systems has been to ignore the interaction beyond some nonbond cutoff. However, for one million particles this requires maintaining an enormous nonbond list and also leads to errors orders of magnitude too large. For periodic systems such cutoffs leads to unacceptable errors, requiring Ewald approaches which *require* Fourier transforms.^{27,28} This leads to a scaling of $N^{1.5}$, totally impractical for systems with million atoms. Because nanoscale simulations require simulations of millions of atoms, we developed methods and optimized parallel computer programs (MPSim) efficient for high capacity MD. Special features include:

- i. Cell Multipole Method²⁹ (CMM) which dramatically reduces the cost of long-range Coulomb and van der Waals interactions while retaining high accuracy. The cost scales linearly with size, allowing atomic-level simulations for million atom systems.^{30–32}

- ii. Reduced Cell Multi-pole Method³³ (RCCM) which handles the special difficulties with long-range Coulomb interactions for crystals by combining a reduced unit cell plus CMM for interaction of the unit cell with its adjacent cells. The cost scales linearly with size while retaining high accuracy, allowing simulation of crystals having a million atoms per unit cell (the major use is for models of amorphous and semi-crystalline materials).
- iii. Newton Euler Inverse Mass Operator method (NEIMO)^{34,35} for internal coordinate dynamics (e.g., treats torsions only). This allows the solution of the dynamical equations for internal coordinates without inverting the mass tensor (moment of inertia tensor). The cost of NEIMO is linear in the number of degrees of freedom and small compared to other costs for million atom systems. More recently we also developed a new constrained force algorithm (CFA) for massively parallel MD simulation of polymers and dendrimer.^{36,37}
- iv. Advanced MD algorithms to simulate systems under constant temperature and constant pressure conditions.^{38–40}
- v. Non-Equilibrium MD: We have implemented synthetic equations of motions to simulate various non-equilibrium conditions to predict transport properties such as viscosity, thermal conductivity of materials.^{41,42} Using these methods, we have studied the shear viscosity of metal alloys and the effect of molecular topology of liquid alkanes on their measured viscosity indices.^{41,43} Examples are given in Sections 4.5 and 4.6.
- vi. Steady state MD methods are used to simulate nonequilibrium processes such as friction and wear in diamond, metals, and metal oxides. Here, the external work is dissipated through material and coupled to a thermal bath using Langevin equation.^{44,45} Examples are given in Sections 4.4 and 4.5.

3. Recent developments in force fields

In this section, we summarize some new developments in classical FF that are capable of describing reactions (bond breaking and forming) and changes in ligancy and coordination for various types of systems.

Section 3.1 summarizes our approach to many-body FF for metals and alloys, which we have applied to studying such properties as moduli, plasticity, viscosity, and phase transformations induced by temperature and stress.^{46–48}

To describe the properties of oxides, ceramics and zeolites, we formulated the FF model (MS-Q) in which the charges change during the dynamics. This is described in Section 3.2. We have used these FF in MD simulations^{49–52} to study a number of partially ionic systems including:

- i. the pressure and stress induced polymorphic phase transitions in silica (see Section 4.7);
- ii. the melt-glass transition and the micro-structure of silica glasses;
- iii. equation of state and melting of corundum (Al_2O_3);
- iv. the phase diagram of MgO;
- v. structure and properties of a large pore zeolite, AlPO_4 .

For covalent systems the MS-Q description is not adequate for describing the dependence of forces on bond order. Hence, we have developed an approach to combine the Abell-Tersoff-Brenner type of valence bond-order dependent potentials with a proper treatment of long-range interactions (electrostatic and van der Waals). This is summarized in Section 3.3.

3.1. Many-body FF for metals and alloys

Recent FF developments for metals have focused on representing the many-body character of forces in metals, which is essential for describing the properties of metallic systems. This has led to empirical many-body potentials known by such names as effective medium theory, embedded atom model, glue model, Finnis-Sinclair (FS) potential, and Sutton-Chen (SC)^{53–56} potential, all of which are widely used in MD simulations of metals. In the SC description the total potential energy of atoms i in the metal is written as

$$E_i = D_o \left[\sum_{j \neq i} V(R_{ij}) - c\rho_i \right]. \quad (1a)$$

Here

$$V(R) = \left(\frac{a}{R} \right)^n \quad (1b)$$

is a pair potential accounting for the short-range repulsion between the atoms i and j , and

$$\rho_i = \sqrt{\sum_j \phi(R_{ij})} \quad (1c)$$

where

$$\phi(R) = \left(\frac{a}{R}\right)^m \quad (1d)$$

is a local density associated with atom i and describing its contribution to cohesion. Here, R_{ij} is the distance between atoms while a is a length scale. C is a dimensionless parameter and D_o is the energy scale, m , and n are integers ($n > m$). In the original parameterization SC considered the cohesive energy and bulk modulus at zero pressure as inputs to determine, D_o , c , n , and m (a is taken as the lattice parameter). Recently, we re-parameterized the SC FF to account for zero point energy and pressure from QM along with fitting phonon frequencies and considering the vacancy formation energy.^{18,41,46–48} This is referred to as quantum Sutton-Chen or Q-SC. In Section 4.6 we apply Q-SC to study the strain rate dependent plastic deformation of a nickel–copper alloy nanowire.

3.2. Reactive FF (MS-Q) for studying ceramics, oxides, zeolite, and minerals

In principle, the phase transitions in minerals and ceramics can be predicted from first principles QM, and significant progress is being made along this line.^{57–59} However, most QM studies have considered only static conditions since dynamical QM simulations are usually not practical for the long times (at least nanoseconds) and large system sizes of interest. Thus, we need to use classical MD to predict such phenomena. The problem here is that standard approaches to FF^{60–63} for ceramics and oxides use simplifications (fixed charges, three-body potentials) that may not be appropriate for describing phase transitions, where the ligancy and structure may change dramatically. For this reason, we have developed an alternative procedure (MS-Q) more likely to describe different phases of ceramics, crystalline polymorphs, melts, and glasses.

Because electrostatics plays an essential role in determining the structure and properties of ceramics, we consider that the first priority of the FF is to produce plausible charges. Since the charges may depend on the distances, angles, and ligancy, the charge must be allowed to readjust to the instantaneous configuration of the atoms. To do this we use the charge equilibration (QEq).⁶⁴ Rather than keeping the charges fixed during the dynamics, as in previous calculations, we now

allow the charges to adjust instantaneously to atomic configuration. We have adjusted the nonelectrostatic FF terms (denoted as MS for Morse-stretch) to be consistent with the variable charges.

The nonelectrostatic interactions (short-range Pauli repulsion, covalency, dispersion, etc.) are included via a simple two-body MS term,

$$U_{ij}^{MS}(R_{ij}) = D_o[e^{\gamma(1-R_{ij}/R_o)} - 2e^{\gamma/2(1-R_{ij}/R_o)}]. \quad (2)$$

The MS parameters for O–O, Si–Si, Al–Al, Mg–Mg, and Si–O, Al–O, Mg–O were optimized to describe the properties (density, cohesive energy, elastic moduli, etc.) of selected polymorphs for each case, α -quartz, stishovite, corundum, and MgO. These FF are transferable and applicable also to minerals, silicates, and zeolites. We refer to this as the MS-Q FF (MS plus charge). We demonstrate the application of these FF in describing glass and quartz-stishovite transformations in Section 4.7.

3.3. Generalized extended empirical bond-order dependent (GEE-BOD) FF for covalent systems

Most FF for organic or covalent bonded systems are developed for ambient conditions and are useful only near equilibrium. They lead to good structures and vibrational frequencies. However, they fail to describe bond breaking and bond formation. An approach to resolve this was developed by Abell⁶⁵ later by Tersoff.^{66–67} To describe all the systems that can be formed by combining C and H provides a significant challenge to such approaches because the possibility of various bond orders drastically affects how the energy depends on structure. A major advance here was made by recently Brenner.⁶⁸ However, the Brenner potential does not describe the long-range nonvalence interactions (electrostatic and dispersion), which are critical for stabilizing molecular crystals of hydrocarbons, graphite, crystal and melt forms of fullerenes, nanotube bundles and multiwall nanotube interactions. Furthermore, these long-range interactions must be included in studying the processes of friction and wear. Recently, we developed a consistent and general approach to include the long-range interactions into bond-order dependent potentials, thus extending the Brenner potential to treat properly both the valence and nonbond interactions.

The Brenner bond-order dependent potential is written as⁶⁸

$$V^B = \sum_i \sum_{j>i} [V_R(r_{ij}) - \bar{B}_{ij} V_A(r_{ij})] \quad (3a)$$

where the sums go over all pairs of atoms. The superscript B indicates the bond-order dependent potential, where V_R describes the repulsive part and V_A describes the attractive part of the pairwise binding potential. Both are taken to have the same form as a general Morse potential,

$$V_R(r_{ij}) = f_{ij}(r_{ij}) \frac{D_{ij}^e S_{ij}}{S_{ij} - 1} \times \exp \left[-\sqrt{2S_{ij}} \beta_{ij} (r_{ij} - R_{ij}^e) \right], \quad (3b)$$

and

$$V_A(r_{ij}) = f_{ij}(r_{ij}) \frac{D_{ij}^e S_{ij}}{S_{ij} - 1} \times \exp \left[-\sqrt{\frac{2}{S_{ij}}} \beta_{ij} (r_{ij} - R_{ij}^e) \right], \quad (3c)$$

where D_{ij}^e , S_{ij} , β_{ij} , and R_{ij}^e , etc., are fitting parameters. Here $f_{ij}(r)$ is a cutoff function that explicitly restricts the interaction to nearby neighbors. $f_{ij}(r)$ is given by a piecewise continuous function

$$f_{ij}(r) = \begin{cases} 1, & r \leq R_{ij}^{(1)} \\ \left\{ 1 + \cos \left[\frac{\pi(r - R_{ij}^{(1)})}{R_{ij}^{(2)} - R_{ij}^{(1)}} \right] \right\} / 2, & R_{ij}^{(1)} < r < R_{ij}^{(2)} \\ 0, & r \geq R_{ij}^{(2)}. \end{cases} \quad (3d)$$

The bond order parameter \bar{B}_{ij} depends on the environment around atom i and j , and implicitly contains many-body terms. Its detailed formulation and parameters are given in Ref. 68.

All interactions of carbon with atoms beyond the four allowed by the Pauli principle lead to very different forces and are referred to as nonbond interactions. This generally leads to short-range repulsion (arising from the Pauli principle) that keeps nonbonded atoms much farther apart than normal bonds (it also includes long-range attraction due to dispersion forces). Thus, we can write the total potential energy of a system as

$$V_{\text{tot}} = \sum_i \sum_j [V_{ij}^B + P(i, j) V_{ij}^{NB}], \quad (4a)$$

where B denotes the bonding or valence terms and while NB denotes the nonbond terms. Here $P(i, j) = P(j, i)$ is an effective screening function that properly accounts for the role of the Pauli principle in limiting the number of bonds. For simplicity, we choose the form of the Pauli screening function as

$$P(i, j) = f(V_{ij}^B, V_{ij}^B) \prod_{k \neq i, j} f(V_{ik}^B V_{kj}^B). \quad (4b)$$

Here, the function $f(x, y)$ has the form

$$f(x, y) = \begin{cases} \exp(-\gamma x^2 y^2) & \text{if } x < 0 \text{ and } y < 0, \\ 1 & \text{otherwise.} \end{cases} \quad (4c)$$

In (4c) γ is scaling parameter, which we have set as $\gamma = 1$. The Pauli screening function eliminates nonbond interaction between two atoms i, j where they are directly bonded (i.e., $V_{ij}^B < 0$) or if they are both bonded to a common atom k (i.e., $V_{ik}^B < 0$ and $V_{kj}^B < 0$). In both cases, the exponential function $P(i, j)$ becomes negligibly small. Hence, the nonbond interactions approach to zero exponentially. This is analogous to the exclusion rules in traditional valence FF.

We refer to the approach in Eq. (4) as the generalized extended empirical bond-order dependent (GEE-BOD) FF. GEE-BOD provides a general method to incorporate nonbond interactions into valence potential in a unified and continuous fashion. Thus, it automatically guarantees energy conservation in MD simulations.

In Section 4.3 we use GEE-BOD to describe double wall nanotubes and in Section 4.4 we use it to describe the friction of rubbing diamond on diamond.

4. Applications of modeling and simulation to nanoscale materials

In this section we will summarize some recent applications to nanoscale systems. This will illustrate the role of the new developments in FF and simulation technology. These applications are:

1. Characterization of SWNTs with accurate (QM derived) FF using MD (Section 4.1).
2. MD studies of alkali doped single-walled nanotubes (Section 4.2).
3. Plastic deformations and mechanical behavior of multi-walled nanotubes (Section 4.3).

4. MD Simulation of Friction and Wear Processes on Diamond (Section 4.4).
5. MD Simulation of Friction and Flow Process for iron oxide slabs separated by 8 nm covered by a SAM and lubricated with $n\text{-C}_{16}\text{H}_{34}$ (Section 4.5).
6. Plastic deformation behavior of metallic nanowires (Section 4.6).
7. Phase behavior of ceramics under compressive loads (Section 4.7).

4.1. Energetics, structure, and mechanical properties of single-walled carbon nanotubes (SWNT)

Carbon nanotubes were discovered in 1991 by Iijima.⁷¹ Since then, there have been many advances in synthesis, in characterization, and in the theoretical understanding of such nanotubes. The novel mechanical and electronic properties of these nanotubes suggest many applications to nanotechnology.

The simplest carbon nanotubes is the single-walled carbon nanotubes (SWNT) which were discovered simultaneously by the Iijima group⁷² and an IBM-Caltch team headed by Bethune.⁷³ These SWNT, which can be regarded as a graphite sheet rolled-up into a cylinder, show remarkable mechanical and electrical properties.⁷⁴ They present tremendous potential as components for use in nanoelectronic and nanomechanical device applications or as structural elements in various composite materials. The original SWNT were isolated amongst a set of other carbon forms. However, Thess and coworkers⁷⁴ have now produced ‘ropes’ of metallic carbon nanotubes having 100–500 SWNTs bundled into a two-dimensional triangular lattice. They have now purified these systems to remove the carbon not involved in SWNT, leading to tightly bundled linear ‘ropes’ of SWNT that are expected to have remarkable mechanical properties, as well as superior electronic and magnetic properties.

Various levels of theory has been used to characterize properties of the SWNT. This includes classical molecular mechanics (MM), lattice dynamics, MD, tight binding QM, and *ab initio* QM methods.^{75–111}

4.1.1. Energetics and the stability of circular versus collapsed tubes

In order to assess mechanical stability of SWNTs, we considered the tubes with three different chiral forms (n, n) armchair, ($n, 0$) zigzag, and ($2n, n$). For diameters less than 60 Å we find that circular SWNT are

most stable, but that larger SWNT collapse into a shape in which the opposite walls in the middle section are 3.4 Å apart (the van der Waals distance) while each end has a nearly circular diameter of ~ 10.7 Å. To mimic long isolated nanotubes, we imposed periodic boundary conditions in the c -direction (tube direction). To eliminate the intertube interactions, we set the cell parameter a and b as 50 times of the circular tube diameter. Energy and structural optimizations were carried out using MPSim.^{30,38}

Figure 2 shows the strain energy per carbon atom versus radius of its circular form. We put the two sets (collapsed and circular) with three chiral forms (n, n) armchair, ($n, 0$) zigzag, and ($2n, n$) on the same plot. For all three forms, there are regions associated with two transition radii (R_1 and R_2). For tubes with a *circular* radius smaller than R_1 , only the circular form is possible, the collapsed initial structure transforms to the circular form during the structural optimization. For tubes with *circular* radii between R_1 and R_2 , there are two stable structures, however the circular structures are still energetically more stable. For tubes with *circular* radius larger than R_2 , the collapsed form becomes energetically favored. The structures and radii of the first transition are:

(n, n) armchair, R_1 is between 10.77 Å of (16, 16) and 11.44 Å of (17, 17),

($2n, n$) chiral, R_1 is between 10.28 Å of (20, 10) and 11.31 Å of (22, 11),

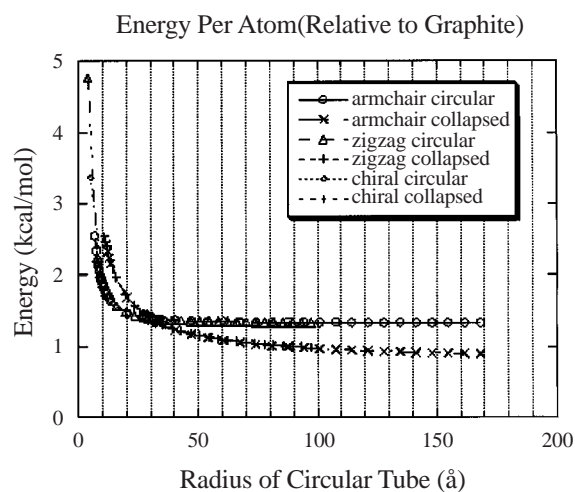


Figure 2. Energy per carbon atom (measured relative to graphite) of stable structures for (n, n) armchair, ($2n, n$) chiral, and ($n, 0$) zigzag SWNTs; R is the radius of corresponding *circular* form.

$(n, 0)$ zigzag, R_1 is between 10.49 Å of (27, 0) and 10.88 of (28, 0),

The structures and the radii of the second transition are:

(n, n) armchair, R_2 is between 29.62 Å of (45, 45) and 30.30 of (46, 46),

$(2n, n)$ chiral, R_2 is between 29.82 Å of (58, 29) and 30.85 of (60, 30),

$(n, 0)$ zigzag, R_2 is between 29.93 Å of (77, 0) and 30.32 of (78, 0).

To extract mesoscale parameters characterizing the basic energetics of tubes, we approximate the tube as a membrane with a radius of curvature R and a bending modulus of κ . Using continuum theory, a tube with wall thickness a and length L has an elastic energy stored of

$$E_{\text{strain}} = \frac{\pi \kappa L a^2}{12R}. \quad (5a)$$

Thus, the energy per atom becomes

$$E_c = \frac{\pi \kappa L a^2}{12RN} + E_o \quad (5b)$$

where N is the number of carbon atoms per slab and E_o is energy per carbon atom for tubes with $R = \infty$ (i.e. flat sheets). Letting $N = 2\pi\rho LR$, where ρ is the number of carbon atoms per unit area of tube wall, we obtain

$$E_c = \kappa \frac{a^2}{24\rho} \frac{1}{R^2} + E_o. \quad (5c)$$

Setting $a = 3.335$ (the spacing between the two graphite sheets) and $R_o = 1.410$ (the C–C bond distance in graphite), and fitting (5) to our calculated energetics leads to an effective sheet modulus of $k(n, n) = 963.44$, $k(n, 0) = 911.6$, and $k(2n, n) = 935.48$ GPa.

The dependence of bending modulus of the sheets on chirality correlates directly with the dependence of transition radius on chirality. Thus, the $(2n, n)$ transition radius is larger than that of the $(n, 0)$ zigzag, but smaller than that of the (n, n) armchair. That is, the higher the bending modulus, the higher the strain energy. The point is that the (n, n) armchair has a higher binding energy than $(2n, n)$, while the $(n, 0)$ zigzag has the lowest binding energy.

The interlayer distances for the collapsed tubes also differ slightly, with $d(n, n) = 3.38$, $d(2n, n) = 3.39$, and $d(n, 0) = 3.41$ (Å). Energetically, interlayer attraction for the armchair is the best with an energy $E_c = 0.7336$ (kcal/mol). This has a stacking of the

opposite walls identical to that in the graphite. The interlayer attraction in the zigzag form is the worst with $E_c = 0.7439$ (kcal/mol); this has the carbon atoms of adjacent layers lined up on top of each other. The energy for the collapsed $(2n, n)$ chiral nanotube is in between.

4.1.2. Structure and mechanical properties of packed SWNT crystals

The armchair SWNT is expected to have the lowest energy for a growing exposed edge and the (10, 10) armchair seems most prevalent experimentally. Good crystals of bucky tubes have not been reported experimentally. However, we have predicted the mechanical properties for crystalline (10, 10) armchair, (17, 0) zigzag, and (12, 6) chiral tubes. These all have similar cross section radii. The MD and MM studies lead to a hexagonal closest packing as the most stable form for all three forms. The triangular lattice parameter for (10, 10) armchair is $a = 16.78$ Å with a density $\rho = 1.33$ (g/cm³). For the (17, 0) zigzag, they are $a = 16.52$ Å, and $\rho = 1.34$ (g/cm³). For the chiral form (12, 6), they are $a = 16.52$ Å and $\rho = 1.40$ (g/cm³).

Using the second derivatives of the potential energy, we determined the Young's modulus along the tube axis for triangular-packed SWNT. They are $Y = 640.30$ GPa, $Y = 648.43$ GPa, and $Y = 673.49$ GPa, respectively. This is smaller than the value of $Y = 1020$ for an isolated graphite sheet, but renormalizing to the projected length of the planes leads to a value within 2% of the graphite value. The difference is only due to the void area along the center of the nanotube (13.5 Å diameter). The detailed study on the vibrational modes, mechanical properties (tensile and compressive strength) of nanotubes are described elsewhere.^{110,111}

4.2. The structure of K-doped SWNT crystals

The development of methods⁷¹ to control the catalytic synthesis of SWNT (originally synthesized by Iijima⁷²) and Bethune et al⁷³ to form ordered ropes containing 100s–1000s of tubes gives hope for developing structures useful for new generations of nanoscale devices. The recent report that these SWNT ropes can be doped to form metallic conductors^{112,113} gives further hope for interesting devices.

There is no data on the structure for such doped systems. To provide this data we started with the predicted minimized crystal structure for armchair (10, 10) SWNT crystals (triangular with $a = b = 16.7$ Å,

$c = 4.94 \text{ \AA}$, $\gamma = 60^\circ$, tube–tube spacing of 16.7 \AA). We allowed up to 6 independent SWNT per unit cell and distributed appropriate numbers of K atoms in various ways. We then carried out 20 ps of MD to equilibrate the system and quenched the structures by minimizing the energy. We then analyzed each case to see if the pattern of K binding sites would suggest new structures to build and minimize. In these studies, we considered both triangular (closest packed tubes) and square packing of the tubes. For triangular crystals with n up to 2, the K intercalates between three tubes, leading to essentially the same spacing as in pristine SWNT. For $n = 3$ –10 the K intercalate between two tubes. This leads to a large increase in lattice spacings for $n = 3$, (at $n = 10$ for spacing is 9.4% larger than for pristine SWNT).

These calculations used the GraFF developed and used for studying K -intercalated fullerenes.¹¹⁴ [It gave accurate results for lattice parameters and other properties for K -intercalated graphite intercalated compounds, (KC_8 and KC_{24}) and K_3C_{60} .]

Figure 3 shows the energy per carbon atom as a function of number of intercalated K ions for two different packing schemes (square and triangular) and different doping types: exo (K atoms allowed only outside the tubes) and endo (K atoms allowed only inside the tubes). Assuming exo K , the global minimum is the triangular structure for $K_5C_{80} = KC_{16}$. The optimum structure has the K packed in the same (2×2) pattern observed for intercalated graphite, KC_8 . The difference for the KC_{16} SWNT is that the K are only on the out-

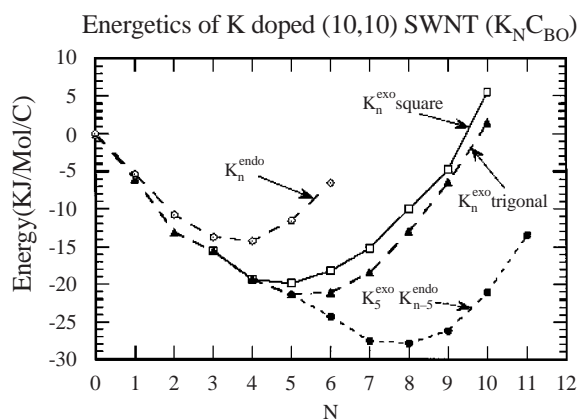


Figure 3. Energy per carbon atom for triangular and square packing of K doped SWNT. For exo doping the optimum is for the triangular structure $K_5C_{80} = KC_{16}$. The square lattice is unstable for K_nC_{80} , $n \leq 2$.

side of the tube (vide infra), leading to half the amount of K . For $n \geq 7$, the K causes significant distortions in the tube shells.

A detailed analysis of structural and vibrational properties of K -doped SWNT is presented in Refs. 111 and 115.

4.3. Mechanical behavior and plastic deformation of multi-walled carbon nanotubes (MWNT)

As an example MWNT, we considered a DWNT consisting of a (10, 10) nanotube is placed inside a (15, 15) nanotube. This leads to a spacing between the tubes of 3.4 \AA , similar to the graphite interlayer separation. In these calculations, we considered the tube to be 20 layers long along the c -axis, leading to 2000 carbon atoms. To calculate the bending modulus, an external force of F was applied in the $-x$ direction to 30 atoms at each end while a force, $2F$, was applied in the $+x$ direction to 60 atoms in the middle of the nanotube, Figure 4. The structure of the DWNT was optimized under various external loads, leading to the energy function in Figure 5. The filled circles were calculated using the original Brenner FF, while the open circles are computed from the GEE-BOD FF. The lines represent quadratic fits to the calculated points. Figure 5 shows that the Brenner potential predicts a bending modulus for MWNT 30% softer than GEE-BOD FF. This difference is mainly due to van der Waals stabilization energy introduced in GEE-BOD between the tubes.

Using a continuum model in the small deformation limit, the energy increase, ΔU , can be written as,

$$\Delta U \cong \frac{1}{E} F^2 \quad (6)$$

where E is the bending modulus and F is the external force.

We subjected the same model system to tensile loads in MD simulation to study the plastic deformation, Figure 6. We find that the DWNT fractures through an unzipping bond breaking process. The energy and force as a function of time for this process is given in Figure 7.

4.4. MD simulation of friction on diamond surfaces

Theoretical investigation of wear and friction is especially important in the design of micro-electromechanical systems (MEMS) and nano-electromechanical systems (NEMS). In order to describe wear, it is essential

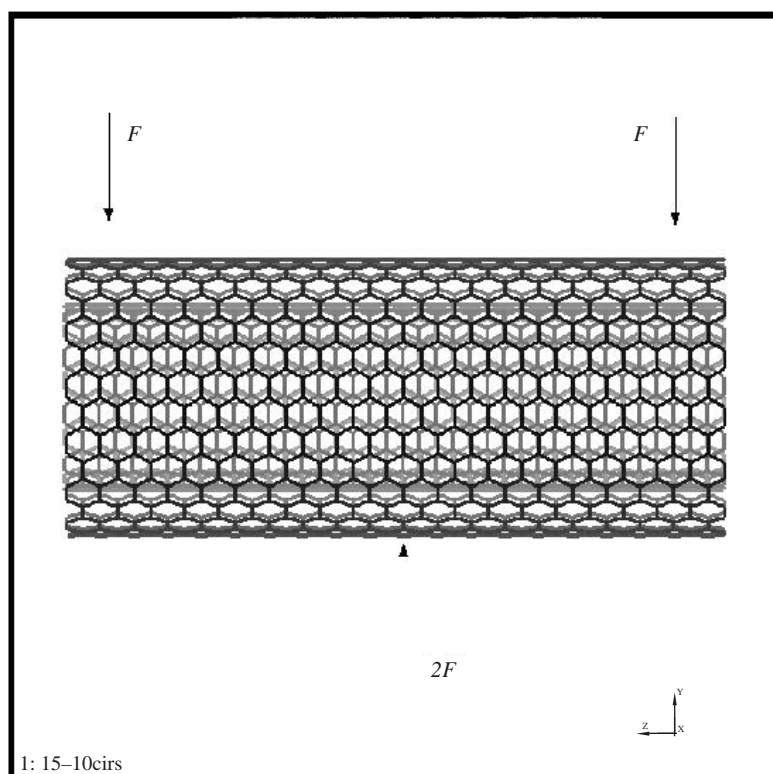


Figure 4. The double wall nanotube [(10, 10 armchair inside (15, 15) armchair] and the distribution of applied forces used in computing the bending modulus of the DWNT.

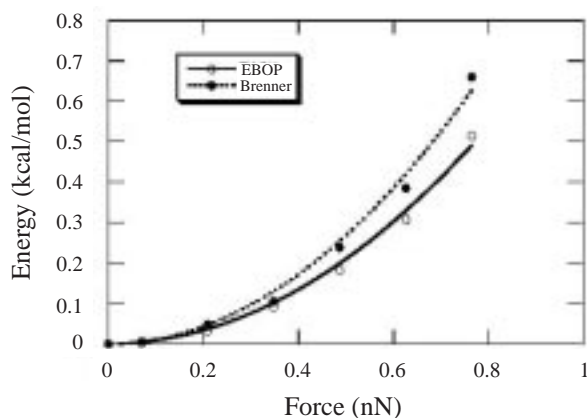


Figure 5. Strain energy as a function of applied force in bending the DWNT.

that the calculations properly describe bond formation and breaking. Thus, we use the GEE-BOD FF.

Low friction is a crucial factor in determining the performance, efficiency, and durability of MEMS.

Because silicon is available in large single crystals which can be etched easily to form micron scale devices, most MEMS are made of silicon. However, Gardos^{116,117} has shown that the friction between such Si systems is very high, leading to very rapid wear. As a result, Gardos proposed that for MEMS involving moving parts one should use diamond. In addition to diamond being the hardest material, polycrystalline diamond (PCD) has a friction coefficient several times smaller than silicon.^{116,117} Since PCD is a potential material for MEMS applications, we studied the friction and wear behavior of diamond surfaces by MD simulations. We used the GEE-BOD in MD simulations to determine the friction coefficients.

We considered the reconstructed (100) surface of diamond, both bare and hydrogenated surfaces. In the simulations, two diamond crystals are put in contact. The bottom two layers of the lower block are held fixed and 2-D periodic boundary condition is applied to represent semi-infinite surfaces. A constant velocity is assigned to the top two layers of the other block. During the simulations, an external force is applied to

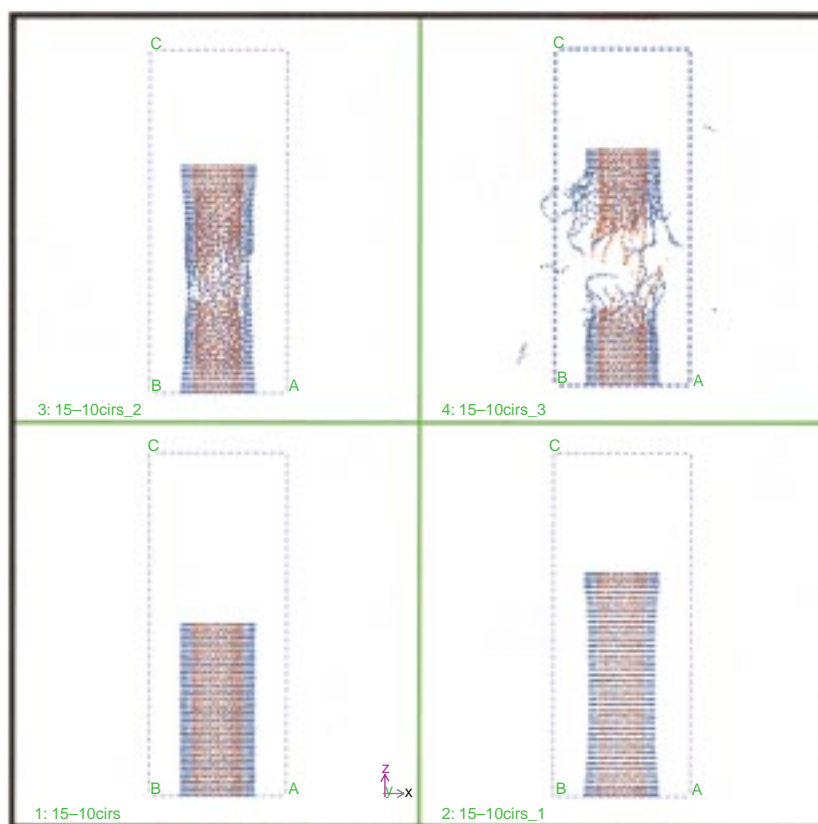


Figure 6. Time evolution of structure under tensile load. A constant strain rate (2%/ps) was applied to the original DWNT structure (lower left). The lower right shows the structure after 15 ps, the upper left after 16 ps (where we see defects appearing), and finally the upper right shows the structure after 18 ps where it has fractured. Note that the fracture occurs by an unzipping of bonds.

maintain the top block at a constant velocity. This force is determined every iteration. The ratio between this average external driving force and average calculated normal force gives the friction coefficient. In order to prevent the system from heating up, a temperature sink is emulated using a stochastic (Langevin) temperature bath.

Figure 8 shows the top view of two hydrogenated diamond $\{100\}$ surfaces. Both surfaces are $C - 2 \times 1$ reconstructed, but they are rotated by 90° with respect to each other. Our simulation considered several specific directions for sliding the top surface over the bottom one. We refer to this as the *differential friction coefficient*. For the system shown in Figure 8, we calculated the differential friction coefficient for three characteristic directions (x , y , and xy). Sliding along the xy direction leads to the lowest resistance, since the path lies along valleys in which the H need not contact. In

contrast, moving in the x and y directions has required the hydrogen atoms to climb over potential barriers.

Figure 9 shows the running average of the force in the normal direction with respect to sliding direction with the sliding velocity maintained at a constant value, 1 Å/ps (100 m/s). The initial oscillations represent the approach a steady state, which usually takes ~ 10 ps. The average normal force is around 850 (kcal/mol)/Å and very similar for different sliding directions. This indicates that differences in the differential friction coefficients arise from differences between the surfaces. Figure 10 presents the running averages of calculated friction coefficients. As we expected, the xy direction has the lowest friction coefficient while the x and y directions are nearly identical. If the two surfaces were perfectly aligned, sliding in the x and y directions would have yielded identical friction coefficients. However, our simulations has the upper block shifted

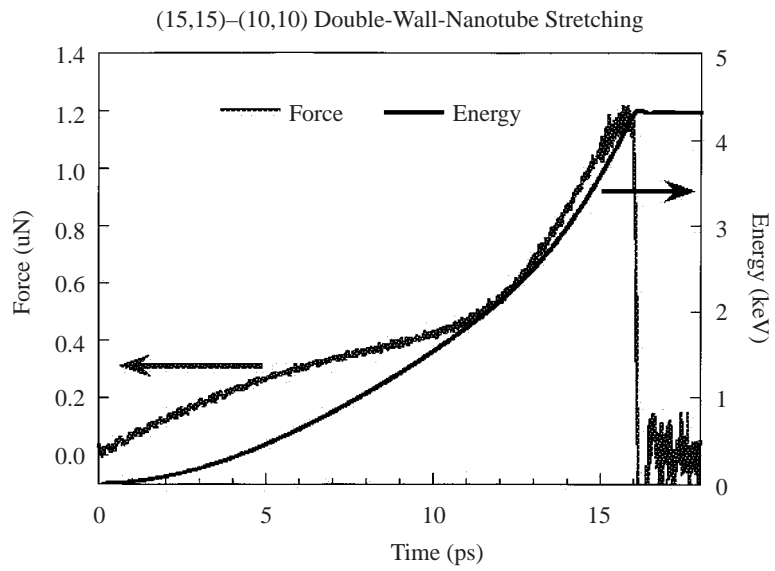


Figure 7. Time evolution of energy and force in tension experiment for DWNT.

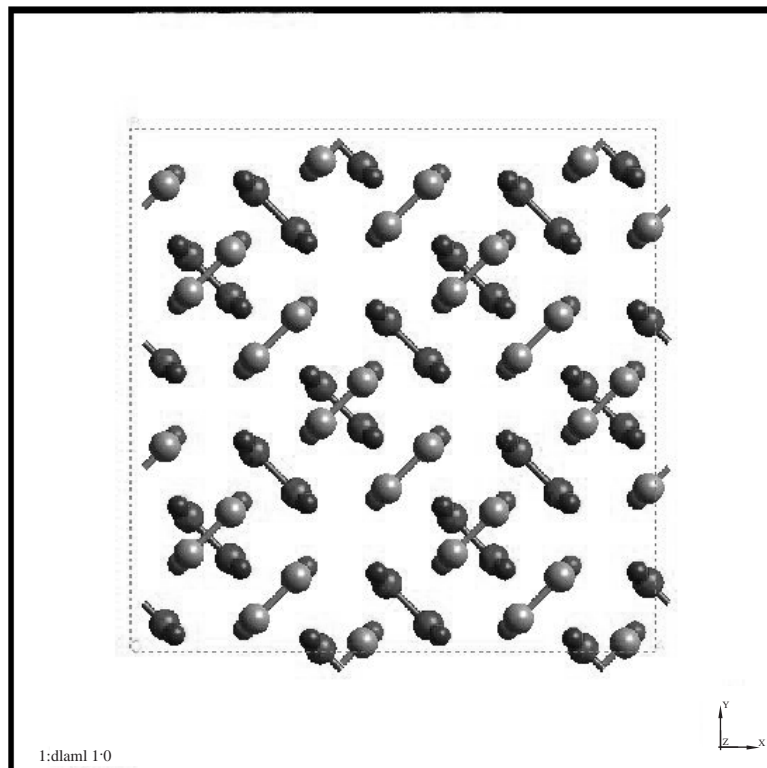


Figure 8. Top view of the hydrogenated $\{100\}$ surfaces of two diamond crystal. Only the atoms at the interface are shown here. The gray and blue atoms are carbon atoms of upper and lower block, respectively. The red and green atoms are hydrogen atoms of upper and lower surfaces, respectively.

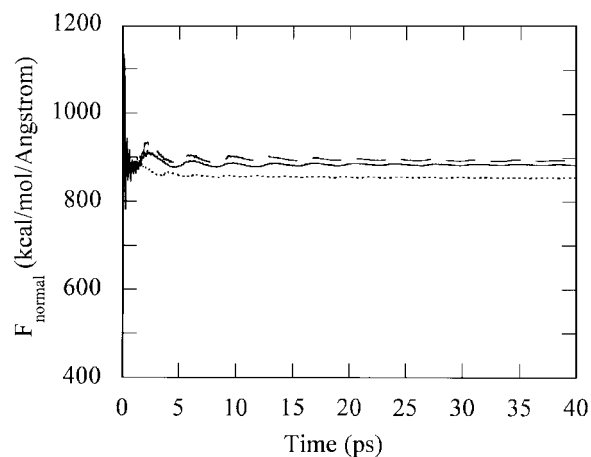


Figure 9. Running average of the normal force for constant sliding speed of 1 (Å/ps) in different directions. The dashed line is the x direction, solid line is the y direction, and dotted line is the xy direction (diagonal).

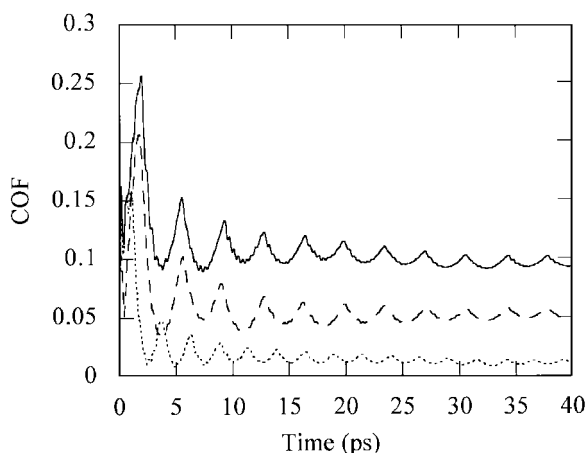


Figure 10. Running average of friction coefficients calculated for different sliding directions. The legend is the same as in Figure 9.

slightly in y direction, giving rise to a smaller friction coefficient than for the x direction.

To compare these results with experiments on single crystals, we must average over all differential friction coefficients. Thus, on (100) surface, we obtain $\mu = 0.1$ for sliding along y -direction, $\mu = 0.05$ for sliding along x -direction and $\mu = 0.01$ sliding along the diagonal xy -direction. Of course for the friction on a PCD we must also average over different crystal orientations.

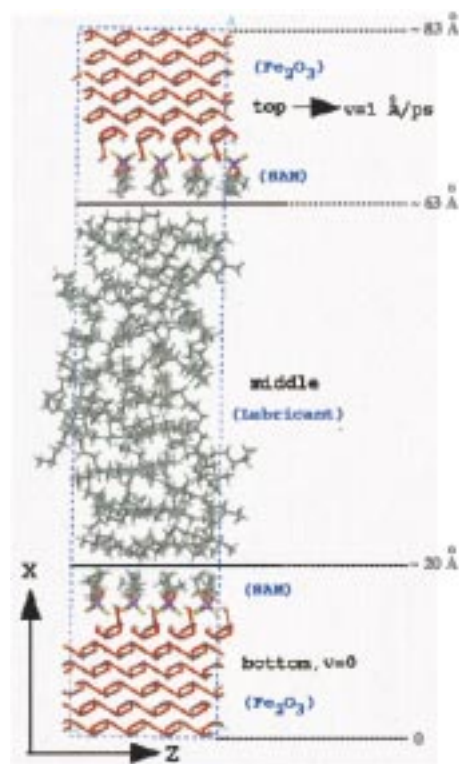


Figure 11. The model system for lubricated slaps separated by 6 nm. The iron oxide slabs are covered with a SAM of DTP (iPr). The lubricant is $n - C_{16}H_{34}$.

4.5. Nanorheology: Friction in lubricated surfaces at nanoscale separations

In order to understand the anti-wear mechanism provided by additives to lubricating oils in engines, we considered a system consisting of two iron oxide slabs each covered by a self-assembled mono-layer (SAM) of wear inhibitor¹¹⁹ [dithiophosphate (DTP) with $R = i - Pr$] with a gap of 4 nm which we filled with $n - C_{16}H_{34}$ lubricant. We then used nonequilibrium MD (NEMD) to study the shear stability and friction of the film at elevated temperatures.

Our calculations used $\alpha - Fe_2O_3$ (001)-(4 × 4) surface as a model for oxidized iron. This surface is composed of periodically arranged rhombohedral 4 × 4 unit cells of lengths 46.56 Å and 26.88 Å along the two diagonals. This unit cell contains 16 Fe binding sites with a Fe-Fe spacing of 5.04 Å. We find that 8 DTP molecules chemisorb to form a SAM, with the S atoms in bridge positions between the Fe atoms (each S is bonded to two nearest neighbor Fe atoms).

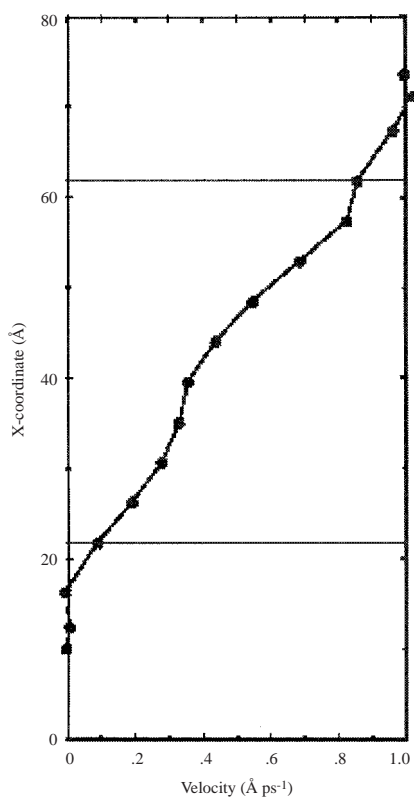


Figure 12. The velocity profile for the lubricant molecules in Figure 11 when the top surface is sliding at 1 Å/ps with respect to the bottom.

To study the friction process between the lubricant and the wear inhibitors, we constructed the model system displayed in Figure 11. In the NEMD the top layer of iron oxide was driven at a constant velocity of 1 Å/ps. The bottom layer was fixed, all other atoms of the Fe_2O_3 , DTP, and lubricant were allowed to move in response to the applied shear (at $T = 300$ K). Figure 12 shows the velocity profile of the lubricant, where we see that the layers of lubricant next to the surface is ordered leading to more slip (lower friction) than the middle layers.

We calculated the normal and lateral forces (in the sliding direction) and evaluated the friction coefficient for this model system. The calculated friction coefficient converges after about 80 ps of simulation, Figure 13. The coefficient of friction is small (0.02) for 0.1 Å/ps larger (0.1) for 1 Å/ps and even larger (0.2) for 10 Å/ps.

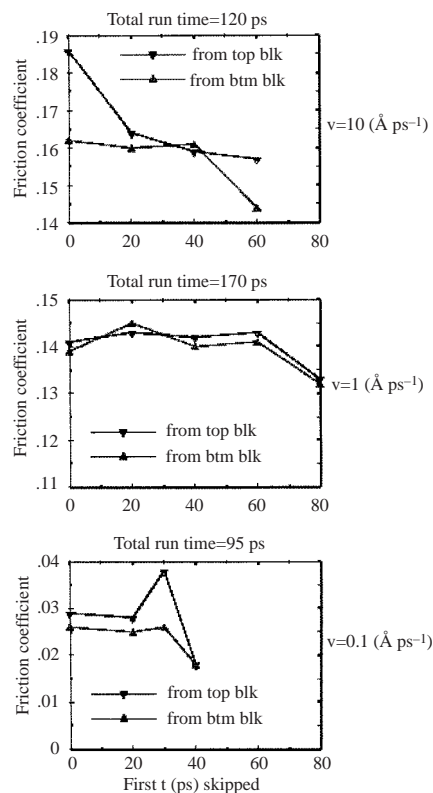


Figure 13. The convergence of the calculated friction coefficient. Friction is measured for both interfaces, top and bottom to check accuracy. These values approach a common value after about 40 ps.

4.6. Plastic deformations in metallic nanowires

We carried out constant strain rate simulations of metallic nanowires using the Q-SC type many-body FF described in Section 3.1. Using 3-D periodic boundary conditions, we constructed model systems containing 1000 Cu and 1000 Ni atoms per cell as a random FCC crystal and equilibrated at 300 K. We then relaxed the system leaving only the c direction as periodic. The other two directions have a finite thickness of 2.0 nm. Thus, we mimicked an infinite CuNi nanowire. To study the plastic deformations, we applied tension to this nanowire at various rates, ranging from 0.005 ps^{-1} to 0.05 ps^{-1} . Due to the small thickness of the system the nanowire cannot sustain dislocations. Rather it undergoes plastic deformation through multiple successive twinning events which harden the wire. For large deformations (100%), the low strain rates lead to necking and fracture of the nanowire.

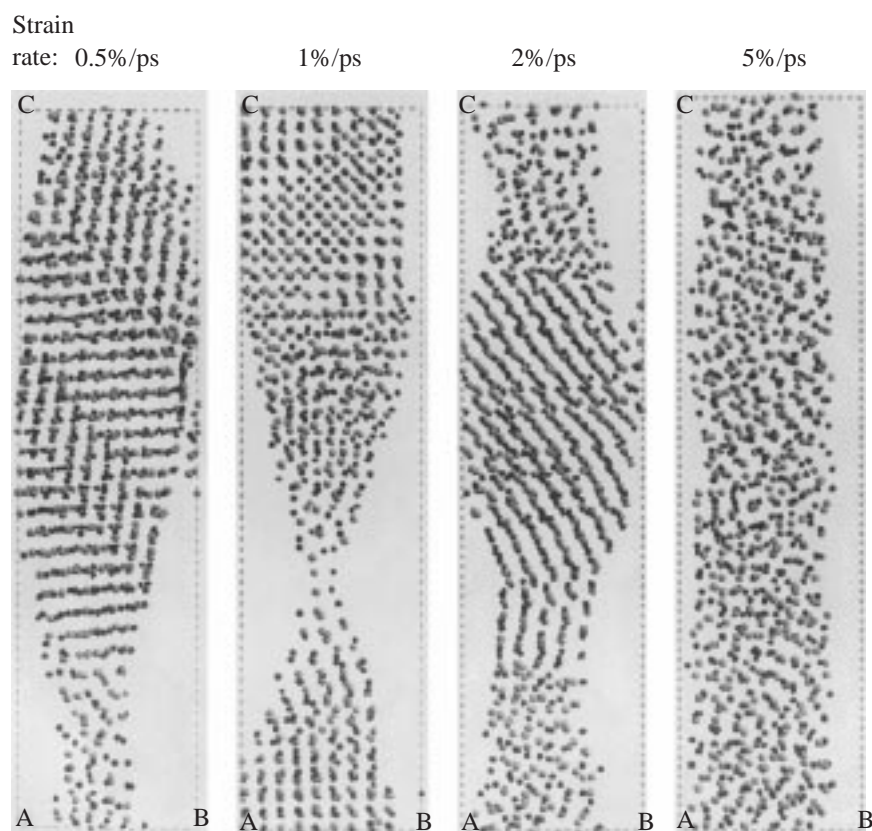


Figure 14. A side view of the Cu Ni nanowire after 100% strain (in the vertical direction). The strain rates were 0.005, 0.01, 0.02, and 0.05 ps^{-1} (THz). The initial width of the cell is 2.0 nm. The lowest strain rate shows multiple twins which lead to hardening. At 0.01 THz there was not sufficient time for twin formation, leading to necking and failure. By 0.05 the system has become an amorphous glass, leading to a uniform nanofiber.

For larger strain rates, the twin size decreases. Ultimately, for the largest strain rates, we observe strain induced amorphization, Figure 14. Here the sample flows like a molten fiber with no necking or fracture. The asymptotic value of tensile stress, σ_{33} , is obtained as 3 GPa. Using this value of tensile stress and strain rate $5 \times 10^{10} \text{ 1/s}$, the calculated apparent viscosity for the sample is, $\eta = 60 \text{ cP}$ (centipoise).

4.7. Pressure induced phase transformations in silica

In recent years, density functional theory and molecular dynamics techniques are increasingly applied in studying the high pressure phases of minerals and ceramics. Especially understanding and interpreting the results of shock wave experiments are of fundamental interest. In these experiments, there is another factor, time

dependence of shock pressure, either by reverberation or impedance occurring in *nanoseconds*. The loading is followed by compression and unloading over longer time scales such as microseconds.

In this section we will describe a study investigating dependence of transition pressure to loading rate and temperature, in pressure induced phase transformation of silica. Pressure induced polymorphic phase transitions in silica are investigated earlier by various researchers, to name a few, Tsuneyuki et al.,¹¹⁹ Vashishta et al.,¹²⁰ Tse and Klug et al.¹²¹ using classical MD approaches, and Binggeli and Chelikowsky¹²² using Quantum Mechanical total energy methods.

Quartz and coesite (both four-coordinate Si) have been observed to transform to stishovite at 15 GPa in shock experiments. To simulate this process we used super cells with 576–640 atoms to describe α -quartz, stishovite, and silica glass [using

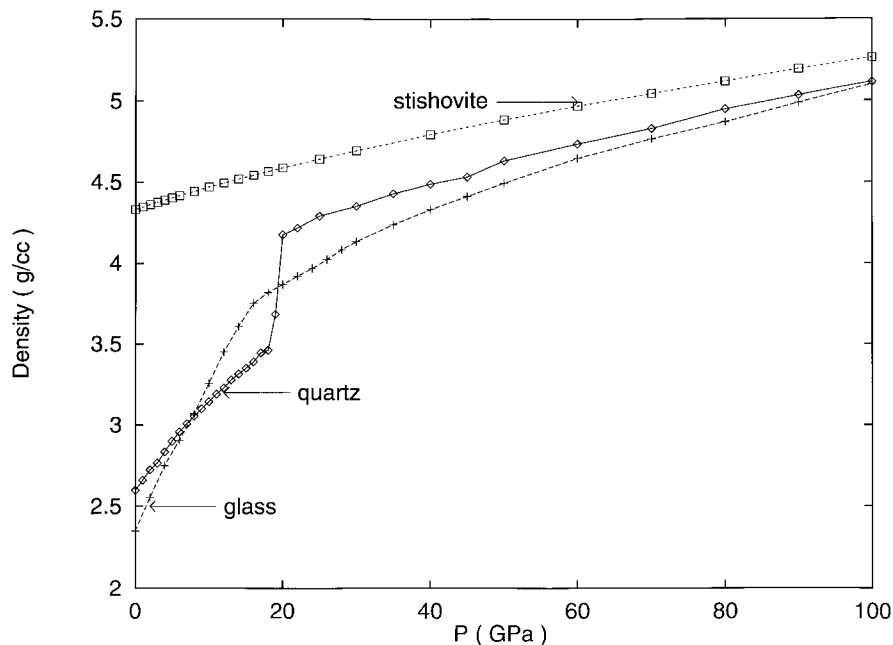


Figure 15. Equilibrium volume per SiO_2 for α -quartz, stishovite, and silica glass as a function of pressure from NPT MD. We started with α -quartz, crystal stishovite and silica glass and used a fixed pressure loading rate of 1.0 GPa/ps at $T = 300$ K. We see a sharp transition at ~ 20 GPa for quartz but a gradual transition from 15 to 120 GPa for glass.

Parrinello-Rahman-*No*se isothermal-isotension (NPT) MD methods^{123,124}].

To investigate the pressure induced phase transformation, we increased the pressure on the system by 1 GPa every pico-seconds for (loading rates of 0.25 GPa/ps and 0.5 GPa/ps led to similar behavior). Figure 15 shows a sharp transition (at 15–20 GPa) from α -quartz to stishovite (containing numerous defects) but the transition from glass to stishovite is quite gradual (17–100 GPa). This was also observed experimentally.^{125–126}

To understand the origin of this difference, we analyzed the average O–Si–O angle as a function of pressure. Starting with α -quartz, we find a dramatic change between 15 GPa and 20 GPa, where the average bond angle changes from nearly all tetrahedral (109.5°) at 15 GPa to mostly octahedral (90°) at 20 GPa. This indicates an abrupt reconstructive structural phase transformation for the crystal.

In contrast for silica the 5- to 6-coordinate local structures emerge slowly as the pressure increases from 20 to 120 GPa. Here the O–Si–O angle distribution changes appreciably between 20 and 30 GPa and continues to change significantly at higher pressures. This indicates a displacive phase transformation for the

glass, requiring diffusion and hence longer times. Even at 100 GPa, the percentage of six-coordinate atoms for silica glass is less than for the structures obtained from quartz. These results are consistent with the interpretation by Stolper and Ahrens¹²⁵ of the experiments.¹²⁶

For α -quartz the 1 GPa/ps loading rate simulations were repeated at higher temperatures (500 K, 700 K, 1000 K, and 1500 K, using a 1 GPa/ps compression rate). We observed that the phase transition changes from 19.5 GPa (300 K), to 16.5 GPa (500 K), to 15.5 GPa (1000 K) and 14.5 GPa for 1500 K. (Probably the temperatures in shock wave experiments range from 1000 to 1500 K.) Experiments¹²⁶ indicate a transition starting at about 14 GPa for 500 K, in reasonable agreement with our result of 16.5 GPa at 500 K.

5. Summary

We described some recent applications of atomistic modeling to carbon nanotubes, diamond surfaces, metallic nanowires, and organic liquids confined to nanoscale slits and structural transitions in ceramics. These simulations use recent developments in force fields for metals, alloys, ceramics, and various phases

of carbon which are also summarized here. This gives some glimpse of the enormous role that theory and modeling is likely to play as nanoscale science becomes a central theme in the 21st century technology.

Acknowledgements

The research projects reported in this paper are supported by grants from DOE-ASCI, NASA/Ames (Computational Nanotechnology grant), NASA-JPL, Owens Corning, and Chevron Research Technology Co. We thank Drs. Yungchan Tang, N. Tom Huff, and Mike Gardos for helpful discussions. The facilities of MSC is also supported by funds from NSF (CHE 95-22179), ARO/DURIP, ARO-MURI, ONR; Asahi Chemical, Avery Dennison, BP Chemical, Beckman Institute, Chevron Petroleum Technology Co., Chevron Chemical Co., Exxon, and Seiko-Epson. We acknowledge the significant contributions of computer time provided by NCSA (Larry Smarr).

References

1. W.A. Goddard III, T.H. Dunning Jr., W.J. Hunt, and P.J. Hay: *Accts. Chem. Res.* 6 (1973): 368.
2. D.J. Tannor, B. Marten, R. Murphy, R.A. Friesner, D. Sitkoff, A. Nicholls, M. Ringnald, W.A. Goddard III, and B. Honig: *J. Am. Chem. Soc.* 116 (1994): 11875.
3. B.H. Greeley, T.V. Russo, D.T. Mainz, R.A. Friesner, J.-M. Langlois, W.A. Goddard III, R.E. Donnelly, and M.N. Ringnald: *J. Chem. Phys.* 101 (1994): 4028.
4. X.J. Chen, J.-M. Langlois, and W.A. Goddard: *Phys. Rev. B* 52 (1995): 2348.
5. S. Dasgupta, T. Yamasaki, and W.A. Goddard III: *J. Chem. Phys.* 104 (1996): 2898.
6. N. Karasawa, S. Dasgupta, and W.A. Goddard III: *J. Phys. Chem.* 95 (1990): 2260.
7. S. Dasgupta, W.B. Hammond, and W.A. Goddard III: *J. Am. Chem. Soc.* 118 (1996): 12291–12301.
8. N. Karasawa and W.A. Goddard III: *Macromolecules* 28 (1995): 6765.
9. N. Karasawa and W.A. Goddard III: *Macromolecules* 25 (1992): 7268.
10. S. Dasgupta, K.A. Brameld, C.F. Fan, and W.A. Goddard III: *Spect. Acta. A* 53 (1997): 1347–1363.
11. S. Dasgupta, K.A. Smith, and W.A. Goddard III: *J. Phys. Chem.* 97 (1993): 10891.
12. C.B. Musgrave, S. Dasgupta, and W.A. Goddard III: *J. Phys. Chem.* 99 (1995): 13321.
13. C.B. Musgrave, S.J. Harris, and W.A. Goddard III: *Chem. Phys. Lett.* 247 (1995): 359.
14. M. McAdon and W.A. Goddard III: *J. Phys. Chem.* 91 (1987): 2607.
15. M. Li and W.A. Goddard III: *J. Chem. Phys.* 98 (1993): 7995.
16. S.L. Mayo, B.D. Olafson, and W.A. Goddard III: *J. Phys. Chem.* 94 (1990): 8897.
17. A.K. Rappé, C.J. Casewit, K.S. Colwell, W.A. Goddard III, and W.M. Skiff: *J. Am. Chem. Soc.* 114 (1992): 10024.
18. Y. Kimura, T. Çağın, Y. Qi, and W.A. Goddard III: *Phys. Rev. B*, submitted.
19. T. Çağın, E. Demiralp, and W.A. Goddard III: *MRS Symp. Proc. Vol. 492* (1998): 287–92.
20. E. Demiralp, T. Çağın, N.T. Huff, and W.A. Goddard III: *Proceedings of XVIII International Congress on Glass*, Eds. M.K. Choudhary, N.T. Huff, C.H. Drummond III, pp. 11–15, July 5–10, 1998, San Fransisco, USA.
21. E. Demiralp, T. Çağın, and W.A. Goddard III: ‘MS-Q Force Fields for Ceramis’, *Phys. Rev. Lett.*, submitted.
22. J.W. Che, T. Çağın, and W.A. Goddard III: ‘Generalized Extended Empirical Bond-Order Potentials with Long Range Interactions,’ *Theo. Chem. Acc.*, in press.
23. T. Çağın and J.R. Ray: *Phys. Rev. A* 37 (1988): 247; T. Çağın and J.R. Ray: *Phys. Rev. A* 37 (1988): 4510.
24. T. Çağın and J.R. Ray: *Phys. Rev. B* 37, 699 (1988); T. Çağın and J.R. Ray: *Phys. Rev. B* 38 7940 (1988); T. Çağın and B.M. Pettitt: *Phys. Rev. B* 39 (1989): 12484.
25. T. Çağın and B.M. Pettitt: *Mol. Phys.* 72 (1991): 111; T. Çağın and B.M. Pettitt: *Mol. Simul.* 5 (1991): 1.
26. T. Çağın (1993) in ‘Computer aided innovation of new materials II’ pp. 255–259, Eds. M. Doyama, J. Kihara, M. Tanaka, and R. Yamamoto.
27. N. Karasawa and W.A. Goddard III: *J. Phys. Chem.* 93 (1989): 7320.
28. Z.M. Chen, T. Çağın, and W.A. Goddard, III: *J. Comp. Chem.* 18 (1997): 1365–70.
29. H.Q. Ding, N. Karasawa, and W.A. Goddard III: *J. Chem. Phys.* 97 (1992): 4309.
30. K.T. Lim, S. Brunett, M. Iotov, R.B. McClurg, N. Vaidehi, S. Dasgupta, S. Taylor, and W.A. Goddard III: *J. Comp. Chem.* 18 (1997): 501–521.
31. M. Iotov, S. Keshihara, S.D. Dasgupta, and W.A. Goddard III: ‘Diffusion of Gases in Polymers’, to be submitted; M. Iotov, Ph.D. Thesis, California Institute of Technology, December 1997.
32. P. Miklis, T. Çağın, and W.A. Goddard III: *J. Am. Chem. Soc.* 119 (1997): 7458.
33. H. Ding, N. Karasawa, and W.A. Goddard III: *Chem. Phys. Lett.* 196 (1992): 6.
34. A.M. Mathiowetz, A. Jain, N. Karasawa, and W.A. Goddard III: *Proteins* 20 (1994): 227.
35. N. Vaidehi, A. Jain, and W.A. Goddard III: *J. Phys. Chem.* 100 (1996): 10508.
36. A. Fijany, T. Çağın, A. J-Botero, and W.A. Goddard III: *Adv. Eng. Software* 29 (1998): 441.
37. A. Fijany, A. J-Botero, and T. Çağın, in *Parallel Computing: Fundamentals Applications and New Directions*, Eds. D’Hollander, G. Joubert, F. Peters, and U. Trottenberg, pp. 505–511 (1998).
38. G. Gao, M. Iotov, T. Çağın, and W.A. Goddard III: ‘MPSim97: Massively Parallel molecular dynamics Simulation program,’ in preparation.

39. T. Çağın, N. Karasawa, S. Dasgupta, and W.A. Goddard III: *Mat. Res. Soc. Symp. Proc.* (1992): 278.
40. T. Çağın, W.A. Goddard III, and M.L. Ary: *Comp. Polymer Sci.* 1 (1991): 241.
41. Yue Qi, T. Çağın, Y. Kimura, and W.A. Goddard III: 'Shear Viscosity of a Liquid Metal Alloy from NEMD: Au-Cu,' *Phys. Rev. E*, submitted.
42. J. Che, T. Çağın and W.A. Goddard, III: 'Thermal conductivity of diamond from NEMD,' in preparation.
43. T. Çağın, P. Miklis, and W.A. Goddard III: 'Effect of molecular topology on the shear viscosity: linear, star and hyper-branched alkanes,' in preparation.
44. T. Çağın, J. Che, M.N. Gardos, and W.A. Goddard III: 'Molecular Dynamics Simulation of friction and wear in diamond application to MEMS and NEMS devices,' unpublished.
45. Y. Zhou, T. Çağın, and W.A. Goddard III: 'Shear stability and friction between lubricants and SAM model of wear inhibitors on iron oxide,' in preparation.
46. Y. Qi, T. Çağın, and W.A. Goddard III: 'Glass formation and Crystallization in Ni : Cu and Cu : Ag alloys' submitted (1998).
47. G. Dereli, T. Çağın, M. Uludoğan, and M. Tomak: *Phil. Mag. Lett.* 75 (1997): 83–102.
48. T. Çağın, G. Dereli, M. Uludoğan, and M. Tomak, 'Thermal and Mechanical properties of some fcc transition metals and their alloys,' *Phys. Rev. B* (1998) submitted.
49. N.T. Huff, E. Demiralp, T. Çağın, and W.A. Goddard III: *Proceedings of XVIII International Congress on Glass*, Eds. M.K. Choudhary, N.T. Huff, C.H. Drummond III, pp. 61–66, July 5–10, 1998, San Fransisco, USA; N.T. Huff, E. Demiralp, T. Çağın, and W.A. Goddard III, 'Molecular dynamics simulations of vitreous silica structures,' *J. Non Cryst. Solids*, submitted.
50. E. Demiralp, Y. Qi, T. Çağın, and W.A. Goddard III: in preparation.
51. A. Strachan, T. Çağın, E. Demiralp, and W.A. Goddard III: 'Phase diagram of MgO from DFT and Molecular Dynamics,' in preparation.
52. O. Kitao, E. Demiralp, T. Çağın, S. Dasgupta, M. Mikami, K. Tanabe, S. Ono, and W.A. Goddard III: *Comp. Mater. Sci.* in press.
53. J.K. Norskov: *Phys. Rev. B* 26 (1982): 2875.
54. M.S. Daw and M.I. Baskes: *Phys. Rev. B* 29 (1984): 6443.
55. M.W. Finnis and J.E. Sinclair: *Phil. Mag.* A 50 (1984): 45.
56. A.P. Sutton and J. Chen: *Phil. Mag. Lett.* 61 (1990): 139.
57. R.E. Cohen, I.I. Mazin, and D.G. Isaac: *Science* 275 (1997): 654.
58. L. Strixrude, R.E. Cohen, R. Yu, and H. Krauker: *Am. Mineral.* 81 (1996): 1293.
59. F. Liu, S.H. Garofalini, D. Kingsmith, and D. Vanderbilt: *Phys. Rev.* 49 (1994): 12528.
60. L.V. Woodcock, C.A. Angell, and P. Cheeseman: *J. Chem. Phys.* 65 (1976): 1565.
61. B.P. Fueston and S.H. Garofalini: *J. Chem. Phys.* 89 (1988): 5818.
62. S. Tsuneyuki, H. Aoki, M. Tsukada, and Y. Matsui: *Phys. Rev. Lett.* 61 (1988): 869.
63. H. Ogawa and Y. Waseda: *Science Reports of The Research Institutes Tohoku University Series A Physics Chemistry and Metallurgy* 36 (1991): 20.
64. A.K. Rappé and W.A. Goddard III: *J. Phys. Chem.* 95 (1991): 3358.
65. G.C. Abel: *Phys. Rev. B* 31 (1985): 6184 .
66. J. Tersoff: *Phys. Rev. Lett.* 56 (1986): 632.
67. J. Tersoff: *Phys. Rev. B* 37 (1988): 6991.
68. D.W. Brenner: *Phys. Rev. B* 42 (1990): 9458.
69. J. Tersoff and R.S. Ruoff: *Phys. Rev. Lett.* 73 (1994): 676–679.
70. R.S. Ruoff, J. Tersoff, D.C. Lorents, S. Subramoney, and B. Chan: *Nature* 364 (1993): 514–516.
71. S. Iijima: *Nature* 354 (1991): 56–58.
72. S. Iijima, C. Brabec, A. Maiti, and J. Bernholc: *J. Chem. Phys.* 104 (1996): 2089–2092.
73. D.S. Bethune, C.H. Kiang, M.S. Devries, G. Gorman, R. Savoy, J. Vazquez, and R. Beyers: *Nature* 363 (1996): 605–607.
74. A. Thess, R. Lee, P. Nikolaev, H. Dai, P. Petit, J. Robert, C. Xu, Y.H. Lee, S.G. Kim, A.G. Rinzler, D.T. Colbert, G.E. Scuseria, D. Tomanek, J.E. Fisher, and R.E. Smalley: *Science* 273 (1996): 483–487.
75. Y.A. Krotov, D.H. Lee, and S.G. Louie: *Phys. Rev. Lett.* 78 (1997): 4245–4248.
76. S. Ihara and S. Itoh: *Surf. Rev. Lett.* 3, (1996): 827–834.
77. N.G. Chopra, L.X. Benedict, V.H. Crespi, M.L. Cohen, S.G. Louie, and A. Zettl: *Nature* 377 (1996): 135–138.
78. M. Menon, E. Richter, and K.R. Subbaswamy: *J. Chem. Phys.* 104 (1996): 5875–5882.
79. N. Hamada, S. Sawada, and A. Oshiyama: *Phys. Rev. Lett.* 78 (1992): 1579–1581.
80. R. Saito, M. Fujita, G. Dresselhaus, and M.S. Dresselhaus: *Appl. Phys. Lett.* 60 (1992): 2204–2206.
81. X. Blase, L.X. Benedict, E.L. Shirley, and S.G. Louie: *Phys. Rev. Lett.* 72 (1994): 1878–1881.
82. B.I. Yakobson, M.P. Campbell, C.J. Brabec, and J. Bernholc: *Comp. Mater. Sci.* 8(5) (1997): 341–348.
83. E. Richter and K.R. Subbaswamy: *Phys. Rev. Lett.* 79 (1997): 2738–41.
84. S. Iijima, C. Brabec, A. Maiti, and J. Bernholc: *J. Chem. Phys.* 104 (1996): 2089–2092.
85. A.M. Rao, E. Richter, S. Bandow, B. Chase, P.C. Eklund, K.A. Williams, S. Fang, K.R. Subbaswamy, M. Menon, A. Thess, R.E. Smalley, G. Dresselhaus, and M.S. Dresselhaus: *Science* 275 (1997): 187–191.
86. H. Chang, W.C. Ermler, and R.M. Pitzer: *J. Phys. Chem.* 95 (1991): 9288.
87. C.-H. Kiang and W.A. Goddard III: *Phys. Rev. Lett.* 76, (1996): 2515.
88. S. Iijima and T. Ichihashi: *Nature*, 363 (1993): 603–605.
89. A. Mansour, S.E. Shnatterly, and J.J. Risko: *Phys. Rev. Lett.* 58 (1986): 614.
90. M.S. Dresselhaus and G. Dresselhaus: *Advances in Physics* 30 (1981): 139.
91. B.J. Garrison and D. Srivastava: *Annu. Rev. Phys. Chem.* 46 (1995): 373.
92. B.J. Garrison, E.J. Dawnkaski, D. Srivastava, and D.W. Brenner: *Science* 255 (1992): 835.

93. D.R. Alfonso, S.E. Ulloa, and D.W. Brenner: *Phys. Rev. B* 49 (1994): 4948.
94. J. Peploski, D.L. Thompson, and L.M. Rapp: *J. Phys. Chem.* 96 (1992): 8538.
95. X. Chang, M.D. Perry, J. Peploski, D.L. Thompson, and L.M. Rapp: *J. Phys. Chem.* 99 (1993): 4748.
96. M.D. Perry and L.M. Rapp: *J. Phys. Chem.* 98 (1994): 4375.
97. R.C. Mowrey, D.W. Brenner, B.I. Dunlap, J.W. Mintmire, and C.T. White: *J. Phys. Chem.* 95 (1991): 7138.
98. D.H. Robertson, D.W. Brenner, and J.W. Mintmire: *Phys. Rev. B* 45 (1992): 12592.
99. D.W. Brenner, J.A. Harrison, C.T. White, and R.J. Colton: *Thin Solid Films* 206 (1991): 220.
100. J.A. Harrison, C.T. White, R.J. Colton, and D.W. Brenner: *J. Phys. Chem.* 97 (1993): 6573.
101. J.A. Harrison and D.W. Brenner: *J. Am. Chem. Soc.* 116 (1994): 10399.
102. M. Vasquez, G. Nemethy, and H.A. Scheraga: *Chem. Rev.* 94 (1994): 2183.
103. J.P. Baremar, G. Cardini, and M.L. Klein: *Phys. Rev. Lett.* 60 (1988): 2152.
104. D.W. Brenner, D.H. Robertson, M.L. Elert, and C.T. White: *Phys. Rev. Lett.* 70 (1993): 2174.
105. P. de Sainte Claire, K. Song, W.L. Hase, and D.W. Brenner: *J. Phys. Chem.* 100 (1996): 1761.
106. A. Omeltchenko, J. Yu, R.K. Kalia, and P. Vashishta: *Phys. Rev. Lett.* 78 (1997): 2148.
107. G. Overney, W. Zhong, and D. Tomanek: *Z. Physics. D* 27, (1993): 93.
108. B.I. Yakobson, C.J. Brabec, and J. Bernholc: *Phys. Rev. Lett.* 76 (1996): 2511.
109. R.S. Ruoff, J. Tersoff, D.C. Lorents, S. Subramoney, and B. Chan: *Nature* 364 (1993): 514.
110. G. Gao, T. Çağın, and W.A. Goddard III: 'Structure, thermodynamic and mechanical properties of nanotubes,' *Nanotechnology* 8 (1998): 183.
111. G. Gao: Thesis (California Institute of Technology, 1998).
112. R.S. Lee, H.J. Kim, J.E. Fischer, A. Thess, and R.E. Smalley: *Nature* 388 (1997): 255.
113. A.M. Rao, P.C. Eklund, S. Bandow, A. Thess, and R.E. Smalley: *Nature* 388 (1997): 257.
114. Y. Guo, N. Karasawa, and W.A. Goddard III: *Nature* 351 (1991): 464; Guo, Y.J. (1992) Ph.D. Dissertation, California Institute of Technology.
115. G. Gao, T. Çağın, and W.A. Goddard III: *Phys. Rev. Lett.* 80, (1998): 5556.
116. M.N. Gardos: *Tribology Letters* 4 (1997): 171.
117. M.N. Gardos: *Tribology Letters*, 2 (1996): 173.
118. S. Jiang, R. Frazier, E.S. Yamaguchi, M. Blanco, S. Dasgupta, Y. Zhou, T. Çağın, Y. Tang, and W.A. Goddard III: *J. Phys. Chem. B* 101 (1997): 7702.
119. S. Tsuneyuki, Y. Matsui, H. Aoki, and M. Tsukada: *Nature* 339 (1989): 209.
120. P. Vashishta, R.K. Kalia, A. Nakana, and W. Jin: *Int. J. Thermophys.* 17 (1996): 169.
121. J.S. Tse and D.D. Klug: *Phys. Rev. Lett.* 67 (1991): 3560.
122. N. Binggeli and J.R. Chelikowsky: *Nature* 353 (1991): 344.
123. M. Parrinello and A. Rahman: *Phys. Rev. Lett.* 45 (1980): 1196; M. Parrinello and A. Rahman: *J. Appl. Phys.* 52 (1981): 7182.
124. S. Nosé: *Mol. Phys.* 52 (1984): 255; S. Nosé, *J. Chem. Phys.* 81 (1984): 511.
125. E.M. Stolper and T.J. Ahrens: *Geophys. Res. Lett.* 14 (1987): 1231.
126. J.W. Swegle: *J. Appl. Phys.* 68 (1990): 1563.